# Turbulence Measurements with the CIRES Tethered Lifting System during CASES-99: Calibration and Spectral Analysis of Temperature and Velocity

ROD FREHLICH, YANNICK MEILLIER, MICHAEL L. JENSEN, AND BEN BALSLEY

*Cooperative Institute for Research in the Environmental Sciences, University of Colorado, Boulder, Colorado*

(Manuscript received 10 July 2002, in final form 15 January 2003)

ABSTRACT

Finescale temperature and velocity measurements with multiple vertically spaced cold-wire and hot-wire sensors on the Cooperative Institute for Research in the Environmental Sciences (CIRES) tethered lifting system (TLS) were produced during the Cooperative Atmosphere–Surface Exchange Study-1999 (CASES-99). The various calibration methods are presented as well as algorithms to extract high-resolution estimates of the energy dissipation rate $\epsilon$ and the temperature structure constant $C_T^2$. The instrumentation is capable of measurements of $\epsilon \approx 10^{-7}$ m$^2$ s$^{-3}$ and $C_T^2 \approx 10^{-6}$ K$^2$ m$^{-2/3}$.

## 1. Introduction

The stable nocturnal boundary layer (NBL) is characterized by a rich collection of waves, interfaces, turbulence, and intermittent processes. The Cooperative Atmosphere–Surface Exchange Study-1999 (CASES-99) was focused on the atmospheric processes of the nocturnal boundary layer near Leon, Kansas (50 km), east of Wichita, Kansas, during the month of October (Poulos et al. 2002). Turbulence in the stable boundary layer and the lower free troposphere have been studied using instrumented towers (Garratt 1981; Nieuwstadt 1984a,b; Gossard et al. 1984; Cuijpers and Kohsiek 1989; Smedman 1988; Smedman et al. 1995), instrumented aircraft (Mahrt 1985; Mahrt and Gamage 1987; Muschinski and Wode 1998), acoustic sounders (Gossard et al. 1984; Smedman 1988), and the Frequency-Modulated Continuous Wave (FMCW) radar, which produces high spatial resolution information on the refractive index structure constant, that is, the level of refractive turbulence (Richter 1969; Gossard et al. 1984; Eaton et al. 1995). Each measurement has its own advantages and disadvantages. However, reliable high-resolution in situ data are critical to observe and validate the many examples of intermittent turbulent processes in the NBL.

One of the most striking examples of intermittent turbulence and waves in the NBL was produced by the FMCW measurements of Gossard et al. (1984) and Eaton et al. (1995). These high-resolution measurements of signal power are proportional to the refractive index structure constant $C_n^2$ if the turbulence has a well-defined inertial range over the sensing volume of the radar at the Bragg wavelength. Gossard et al. (1984) determined that a smoothly varying interface of refractive index can produce detectable radar backscatter, which could be incorrectly interpreted as a region of high $C_n^2$ from Bragg scattering. The in situ turbulence measurements of the tethered lifting system can answer these questions (Balsley et al. 2003).

Another important aspect of stable nighttime turbulence is the ''global intermittency'' (Mahrt 1989), that is, variations in space and time of the finescale turbulence quantities, such as the energy dissipation rate $\epsilon$ and the temperature structure constant $C_T^2$. Accurate in situ measurements of the spatial and temporal variability of $\epsilon$ are essential for valid comparison with other remote sensing techniques for estimating $\epsilon$, such as Doppler radar (Cohn 1995; Jacoby-Koaly et al. 2002) and Doppler lidar (Frehlich et al. 1998). The large-scale variations of global intermittency also affect the interpretation of the small-scale statistics of turbulence (Sreenivasan and Stolovitzky 1996; Alisse and Sidi 2000; Danaila et al. 2002). In addition, similarity properties of structure constants in stable conditions can produce estimates of temperature and momentum flux, as well as the local Obukhov length (Wyngaard and Kosovic 1994). Muschinski and Lenschow (2001) have produced an overview of the various research needs in the area of finescale turbulence. Some of these needs have been addressed by the CASES-99 campaign (Poulos et al. 2002).

In situ measurements of the small-scale turbulence is typically performed with fixed sensors on towers or on moving platforms such as aircraft and helicopter (Mus-

*Corresponding author address:* Dr. Rod Frehlich, CIRES, University of Colorado, Campus Box 216, Boulder, CO 80309-0216.
E-mail: rgf@cires.colorado.edu

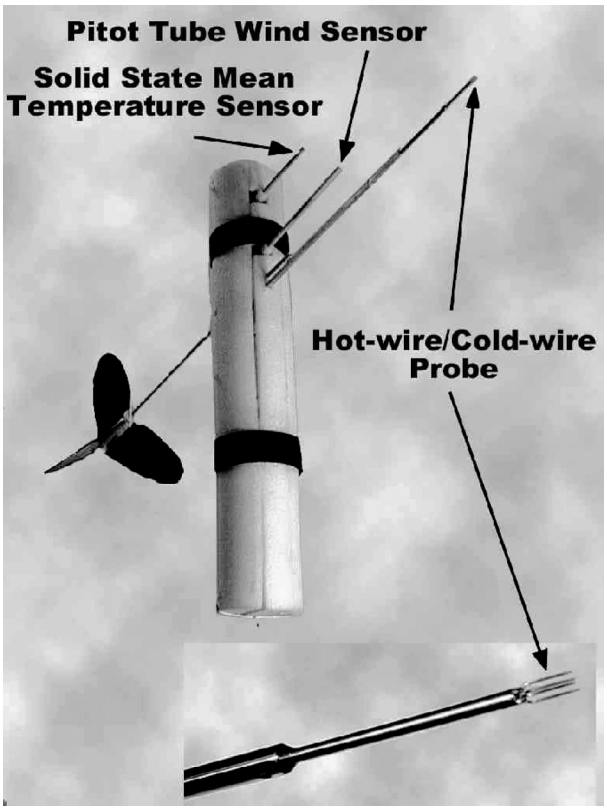


FIG. 1. Photograph of the turbulence sensor package indicating the low-frequency temperature sensor, the Pitot-tube wind speed sensor, and the hot-wire/cold-wire high-frequency probe.

chinski and Wode 1998). Both measurements are limited in their altitude coverage and aircraft provide only a single measurement. In addition, measurements from a fast-moving platform require higher bandwidth and lower noise than the same measurements from a slow-moving platform to sample a given regime of spatial scales (Muschinski et al. 2001).

The tethered lifting system (TLS) was developed by the Cooperative Institute for Research in the Environmental Sciences (CIRES) at the University of Colorado for a variety of atmospheric measurements (Balsley et al. 1998, 2003; Muschinski et al. 2001). The relatively stable windspeed in the nocturnal jet is ideally suited for the operation of the kite system while low windspeed conditions is ideal for the tethered blimp. A vertical array of turbulence sensors was specifically designed for the CASES-99 campaign to produce finescale temperature and velocity measurements at a fixed altitude and also to produce profiles of atmospheric quantities up to an altitude of 2 km (see Fig. 1). The temperature measurements were produced with a low-frequency response solid-state temperature sensor and a high-frequency response fine cold-wire sensor. The velocity measurements consisted of a sensitive Pitot-tube velocity sensor vaned into the wind and a high-frequency response fine hot-wire sensor. The fine-wire sensors were chosen to provide the most robust mechanical lifetime, that is, a tungsten wire with a diameter of 5 $\mu$m, a length of 1.5 mm, and a typical resistance of 4$\Omega$. The diameter of the cylindrical sensor package is 10 cm and the length of the supports for the hot-wire/cold-wire sensor is 40.6 cm to reduce the effects of flow distortion (Miller et al. 1999; see Fig. 1). The data was recorded with 12 bits on onboard compact flash disks and downloaded to a PC after each flight. During the campaign, there were 11 flights of 3–10-h duration. For each flight, the high-frequency turbulence data consisted of many records of 180 s of continuous data separated by a 9-s gap to write the data to the compact flash disk. To provide accurate measurements of the finescale fluctuations, each signal was split into a low-frequency component and an amplified high-frequency component, which is ideally suited for the analysis of small-scale turbulence. Note that triple hot-film anemometers were deployed at a surface tower during the CASES-99 campaign (Skelly et al. 2002).

Accurate calibration of the fine-wire sensors is difficult in the field because the changing atmospheric conditions alter the properties of the wire. This is especially critical for the calibration of the hot-wire sensors. Therefore, calibrations were performed with simultaneous independent low-frequency measurements of temperature and velocity. The low-frequency temperature sensor (see Fig. 1) is located 33 cm from the cold-wire sensor (15.2 cm vertical and 29.2 cm horizontal) and the Pitot tube is located 22.5 cm from the hot-wire sensor (6.4 cm vertical and 21.6 cm horizontal). In past campaigns (Muschinski et al. 2001), the high-frequency signal was calibrated assuming a calibration constant for the fluctuations based on a linear approximation to the low-frequency calibration data. Here, we propose a more accurate calibration that merges the low- and high-frequency information into a reconstructed signal.

The calibration procedure will be discussed as well as methods for estimating the temperature and velocity structure constants that describe the small-scale turbulence. The structure constants are attractive because they have good statistical properties, that is, many independent spectral estimates can be produced with short lengths of data, which produces accurate estimates (Smalikho 1997). However, local isotropy and Taylor's frozen hypothesis is required for accurate estimates. These assumptions will be investigated in detail to evaluate the performance of the TLS for high-resolution turbulence measurements.

## 2. Merging the low-frequency and high-frequency signals

For both the temperature and velocity, the total signal $x(t)$ consists of a low-frequency component $y(t)$ and a high-frequency component $z(t)$. The total signal is recovered using a merging algorithm in the frequency

domain. The Fourier transform $X(f)$ of time series $x(t)$ is given by

$$X(f) = \int_{-\infty}^{\infty} e^{-2\pi i f t} x(t)\, dt, \tag{1}$$

with an inverse Fourier transform

$$x(t) = \int_{-\infty}^{\infty} e^{2\pi i f t} X(f)\, df. \tag{2}$$

The Fourier transform $X_{LF}(f)$ of the low-frequency signal is

$$X_{LF}(f) = H_{LF}(f) X(f), \tag{3}$$

where $H_{LF}(f)$ is the transfer function of the low-frequency signal $x_{LF}(t)$.

Similarly, the Fourier transform $X_{HF}(f)$ of the high-frequency signal is

$$X_{HF}(f) = H_{HF}(f) X(f), \tag{4}$$

where $H_{HF}(f)$ is the transfer function of the high-pass filter given by

$$H_{HF}(f) = G_{HF}\left[\frac{2\pi i \tau_{HF} f}{1 + 2\pi i \tau_{HF} f}\right]^2, \tag{5}$$

where $G_{HF}$ is the gain of the high-pass circuit compared with the low-frequency signal component and $\tau_{HF} = 4.99$ s for the temperature and velocity electronic circuit.

The sampling interval $\Delta_{LF}$ for the low-frequency signal is an integral multiple of the sampling interval $\Delta_{HF}$ for the high-frequency signal, which produces equal frequency resolution when the total observation times are equal; that is, $T = \Delta_{LF} M_{LF} = \Delta_{HF} M_{HF}$, where $M_{LF}$ and $M_{HF}$ are the number of points for the low-frequency and high-frequency data, respectively. Typically, $\Delta_{LF} = 1.0$ s, $\Delta_{HF} = 0.005$ s, and $M_{HF} = 200\, M_{LF}$.

The complete Fourier transform $X(f)$ is produced by merging the corrected Fourier transforms from the two signals; that is,

$$X(f) = \begin{cases} \dfrac{X_{LF}(f)}{H_{LF}(f)} & f < f_1, \\ \dfrac{X_{HF}(f)}{H_{HF}(f)} & f > f_1, \end{cases} \tag{6}$$

and the merging frequency $f_1$ is chosen as the center of the overlap region. The merging frequency $f_1$ was typically chosen as 0.01 Hz to emphasize the higher-quality high-frequency signal, which was digitized with more significant bits. The reconstructed signal $x(t)$ is produced by the inverse Fourier transform. Accurate merging requires that the spectral signal power is much larger than the spectral noise power in the overlap region around the frequency $f_1$. This merging techniques was applied to the temperature and velocity measurements.

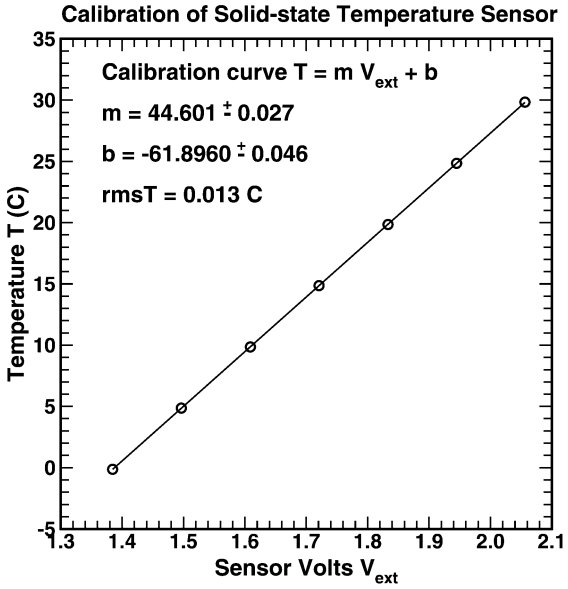


FIG. 2. Calibration curve for the solid-state temperature sensor.

## 3. Temperature measurements

The high-frequency temperature measurements were produced by operating the tungsten wire with a constant current of 2 mA. The voltage across the tungsten wire was amplified and split into two output voltage signals: a low-frequency signal $v_{LF}(t)$ and a high-frequency signal $v_{HF}(t)$. The high-frequency signal had a high-pass filter with a time constant of 4.99 s and a low-pass filter with a 3-dB bandwidth of 488 Hz. The low-frequency signal $v_{LF}(t)$ and the solid-state external temperature signal $V_{ext}(t)$ (Analog Devices AD22100) were sampled simultaneously at 1 Hz. The solid-state sensor was calibrated in the National Center for Atmospheric Research (NCAR) calibration facility (see Fig. 2) and had excellent linearity and accuracy over the typical temperature range experienced during CASES-99. The largest deviation from the best-fit straight line is 0.0223 K. A radiation shield was placed around the solid-state temperature sensor to improve the absolute accuracy of the temperature measurements.

The high-frequency voltage signal $v_{HF}(t)$ was typically sampled at 200 Hz. The total temperature signal $x(t)$ was produced by merging the calibrated external temperature signal $T_{ext}(t)$ with the calibrated high-frequency temperature signal $x_{HF}(t)$, where

$$x_{HF}(t) = G_{CW}\, v_{HF}(t), \tag{7}$$

and the cold-wire (CW) calibration constant $G_{CW}$ must be determined for each tungsten wire. Because the radiation shield around the solid-state temperature sensor produced some error with changing conditions, a spectral technique was used to estimate the calibration constant $G_{CW}$; that is, the fluctuations in the temperature signals were used for calibration instead of a long-term average of the signals.

*Spectral calibration method*

The calibration constant $G_{CW}$ can be estimated by relating the external temperature signal to the low-frequency voltage signal in the low-frequency region. The Fourier transform $T_{ext}(f)$ of the low-frequency temperature signal is given by Eq. (3):

$$T_{ext}(f) = H_{LF_{ext}}(f)X(f), \tag{8}$$

where

$$H_{LF_{ext}}(f) = \frac{1}{1 + 2\pi i\tau_{LF_{ext}}f}, \tag{9}$$

and $\tau_{LF_{ext}} = 25$ s was determined by the time constant of the external temperature signal as the sensor passed through sharp temperature interfaces (e.g., Fig. 4).

The Fourier transform of the low-frequency cold-wire signal $v_{LF}(t)$ is given by Eq. (3):

$$V_{LFCW}(f) = K_{CW}H_{LFCW}(f)X(f), \tag{10}$$

where $K_{CW}$ is the sensitivity of the cold-wire and,

$$H_{LFCW}(f) = \frac{1 + R_{LF} + 2\pi i\tau_{LF}f}{(1 + R_{LF})(1 + 2\pi i\tau_{LF}f)}, \tag{11}$$

where $R_{LF} = 100.0$ and $\tau_{LF} = 0.1$ sec. The calibration constant $G_{CW}$ for the high-frequency signal is given by

$$G_{CW} = \frac{K_{CW}}{G_{HF}}, \tag{12}$$

where $G_{HF} = 705.334$ is the gain of the high-pass circuit compared with the low-frequency signal $v_{LF}$.

Solving Eqs. (8) and (10) for $X(f)$ and equating the results produces

$$\frac{T_{ext}(f)}{H_{LF_{ext}}(f)} = \frac{K_{CW}V_{LFCW}(f)}{H_{LFCW}(f)}, \tag{13}$$

which can be written in spectral form as

$$S_{LF}^{1/2}(f) = K_{CW}\, S_{LFCW}^{1/2}(f), \tag{14}$$

where

$$S_{LF}(f) = \frac{|T_{ext}(f)|^2}{|H_{LF_{ext}}(f)|^2} \tag{15}$$

is the spectrum of the temperature signal from the solid-state sensor, and

$$S_{LFCW}(f) = \frac{|V_{LFCW}(f)|^2}{|H_{LFCW}(f)|^2} \tag{16}$$

is the spectrum of the temperature signal from the cold-wire signal. The slope of $S_{LF}^{1/2}(f)$ versus $S_{LFCW}^{1/2}(f)$ is $K_{CW}$ [note that $S_{LF}^{1/2}(f)$ and $S_{LFCW}^{1/2}(f)$ have a correlation coefficient of unity if the additive noise is negligible]. The error in the best-fit slope provides an estimate for the error in the calibration constant $G_{CW}$. The results of this analysis is shown in Fig. 3 and $G_{CW} = 0.5887 \pm 0.0026$, that is, an accuracy of 0.44%. The traditional method of calibration based on the average external temperature and the average of the low-frequency voltage signal produced $G_{CW} = 0.5776 \pm 0.0058$, which has less accuracy than the spectral method.

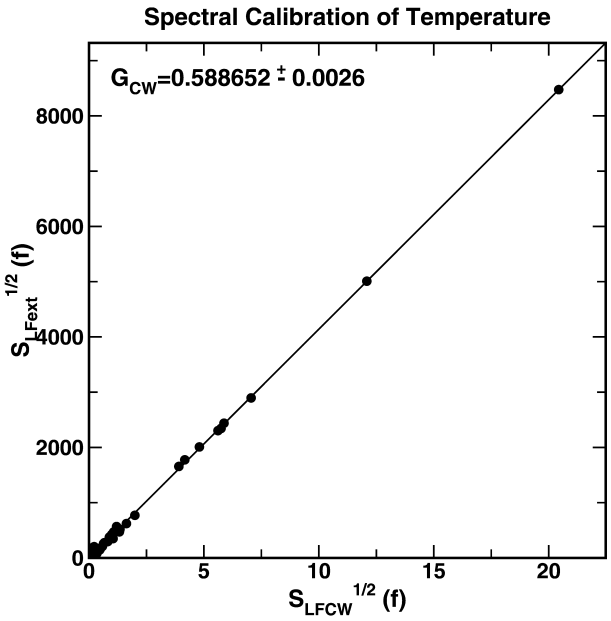


FIG. 3. Spectral calibration of the cold-wire temperature signal.

The calibrated high-frequency temperature signal $x_{HF}(t)$ is given by Eq. (7). This signal is merged with the calibrated low-frequency external temperature signal $T_{ext}(t)$ using the algorithm in section 2. Results of the merging are shown in Fig. 4 for a slow transect through a sharp temperature gradient (Balsley et al. 2003). The absolute accuracy of all the temperature data is better than 0.5 K and the accuracy of all the calibration constants $G_{CW}$ is better than 2%, based on the error in the best-fit slope of the calibration curves (see Fig. 3).

## 4. Velocity measurements

Hot-wire (HW) velocity measurements were produced to provide accurate measurements of the finescale turbulence. The tungsten wire was oriented along the vertical axis and operated with an overheat ratio of 1.8. The output voltage was split into two signals: a low-frequency signal $x_{LF}(t)$ and a high-frequency signal $x_{HF}(t)$ (note that the same notation was used for the temperature measurements). The total voltage signal $x(t)$ was produced with the merging algorithm of section 2. The low-frequency transfer function Eq. (3) is

$$H_{LFHW}(f) = \frac{1 + \pi i\tau_{LF}f}{1 + 2\pi i\tau_{LF}f}, \tag{17}$$

and $\tau_{LF} = 0.1$ s.

The high-frequency transfer function is given by Eq. (5), where $G_{HF} = 8.7406$ and $\tau_{HF} = 4.99$ s based on the electronic circuit.

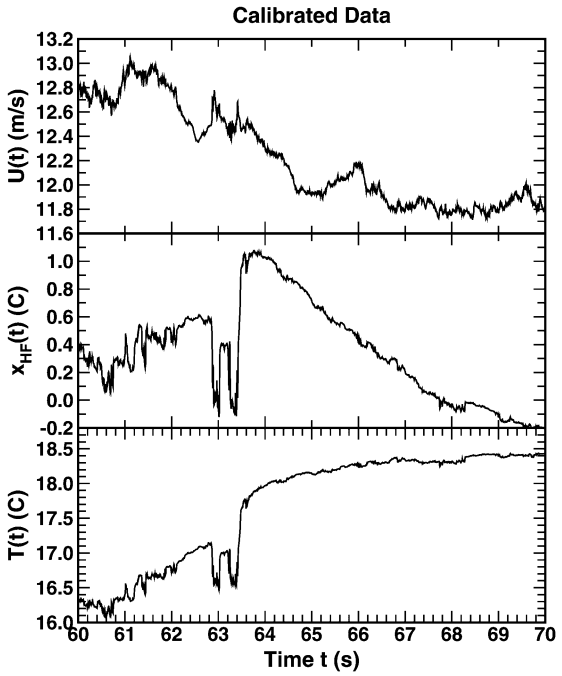


FIG. 4. Calibrated hot-wire velocity $U(t)$, temperature $T(t)$, and high-pass temperature fluctuations $x_{\mathrm{HF}}(t)$ vs time $t$.

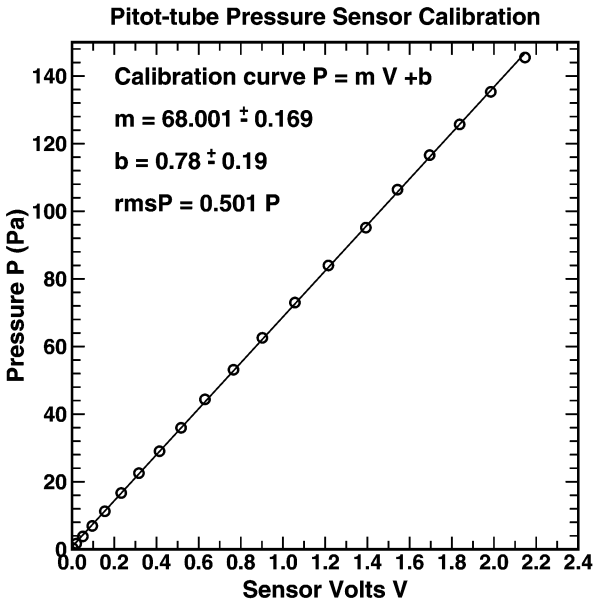


FIG. 5. Calibration curve for the Pitot-tube pressure sensor.

The calibrated velocity $U(t)$ was produced by applying the modified King's law to the reconstructed hot-wire signal $x(t)$ (Bruun 1995; Hugo et al. 1999); that is,

$$x(t)^2/(T_w - T) = c + d\rho^n U(t)^n, \tag{18}$$

where $T_w - T$ is the temperature difference of the hot-wire; $\rho$ is the density of air; and $c$, $d$, and $n$ are empirically determined parameters. The calibrated hot-wire velocity is then

$$U(t) = \frac{1}{\rho d^{1/n}}\left[\frac{x(t)^2}{T_w - T} - c\right]^{1/n}. \tag{19}$$

The calibration of fluctuating velocity in Muschinski et al. (2001) used the slope of the King's law curve instead of the reconstructed voltage signal.

Unfortunately, the constants in King's law can vary with conditions, especially the age and surface conditions of the wire. Therefore, velocity calibrations were produced with simultaneous measurement of the horizontal velocity from a Pitot tube vaned into the wind. The dynamic pressure P induced at the end of a Pitot tube is

$$P = \rho U_{\mathrm{pitot}}^2/2. \tag{20}$$

The Pitot-tube pressure sensor is a silicon micromachined solid-state sensor (Data Instruments DCXL01DN) and the output voltage $V$ was calibrated in the NCAR wind tunnel (see Fig. 5). The pressure sensor measures the difference between the total pressure at the end of the Pitot tube and a reference pressure chosen as the center of the aerodynamic package. It is critical that the aerodynamic package have a robust design so that the reference pressure does not change with conditions.

The constants of King's law ($c$, $d$, $n$, $T_w$) were determined by minimizing the mean-square error between the Pitot-tube velocity $U_{\mathrm{pitot}}$ and the predicted hot-wire velocity $U_{\mathrm{hw}}$ using the low-frequency signal $y(t)$ in King's law Eq. (19). The time intervals for a King's law fit was typically longer than 6 min and shorter than 30 min. An example of the King's law fit is shown in Fig. 6 for 12 min of data. The scatter in the fit is from four main sources: the difference in the bandwidth of the two measurements, the 22.5-cm separation between the two measurements, errors in the angle of the vane, and the additive noise in the sensors.

The final calibrated velocity $U(t)$ was produced from the merged hot-wire voltage signal $x(t)$ (see section 2) using Eq. (19) (see Fig. 4). An example of the corrected spectra of the low-frequency and high-frequency signals is shown in Fig. 7.

## 5. Velocity spectra

The hot-wire velocity is essentially a measurement of the horizontal velocity $V_H(t)$, which can be written as

$$V_H(t) = [U(t) + v(t)]^{1/2} \approx U_0 + u(t) + \frac{v^2(t)}{2U(t)}, \tag{21}$$

where $U(t)$ is the longitudinal velocity, $v(t)$ is the transverse velocity, $U_0$ is the local mean velocity, and $u(t)$ is the fluctuations in the longitudinal velocity. The one-dimensional spectrum $S_u(f)$ of the longitudinal velocity fluctuations is an important statistic for the velocity field. If the last term of Eq. (21) can be neglected, then

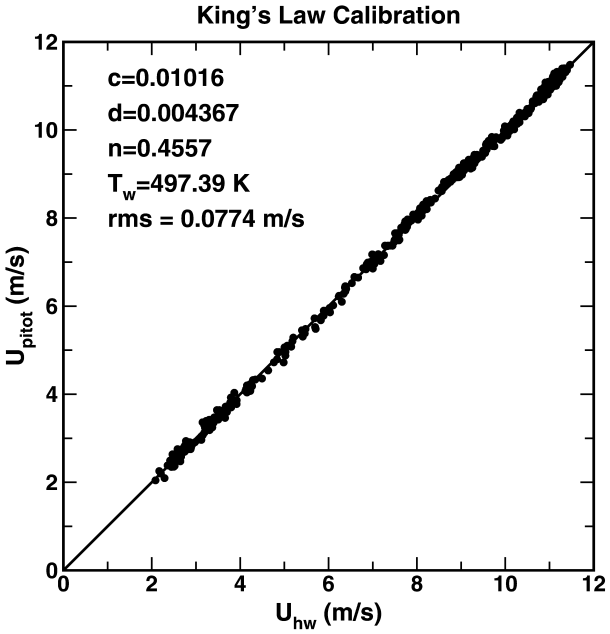


FIG. 6. Comparison of hot-wire velocity $U_{\rm hw}$ from best-fit King's law Eq. (19) and Pitot-tube velocity $U_{\rm pitot}$.

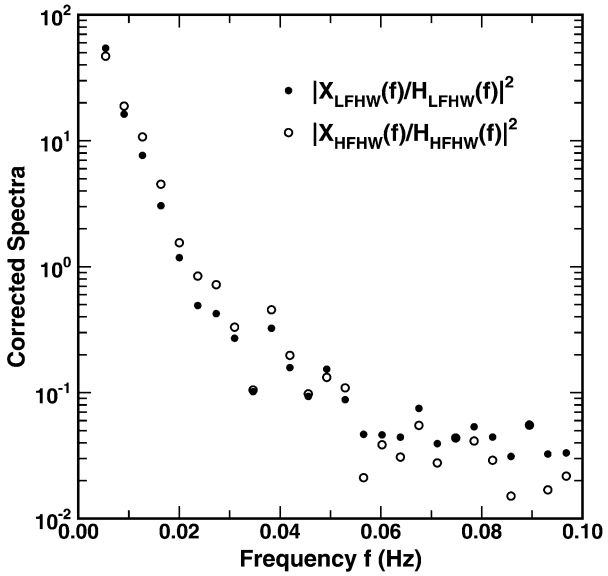


FIG. 7. Spectra of corrected low-frequency spectrum $|X_{\rm LFHW}(f)/H_{\rm LFHW}(f)|^2$ (bullet) and high-frequency spectrum $|X_{\rm HFHW}(f)/H_{\rm HFHW}(f)|^2$ (open circle) for hot-wire signal. The spectra have been averaged in frequency for a clearer display.

the hot-wire velocity is the longitudinal velocity $U(t)$. This is an excellent approximation especially for the calculation of higher-order statistics such as the spectrum $S_u(f)$.

The fast Fourier transform (FFT) estimate of the raw spectrum of the longitudinal velocity $u(t) = u(m\Delta_t)$ is

$$S_u(n\Delta_f) = \frac{2\Delta_t}{M}\left|\sum_{m=0}^{M-1} u(m\Delta_t)e^{-2\pi inm/M}\right|^2, \qquad (22)$$

which is normalized such that the integral of $S_u(f)$ over positive frequency is the variance of $u(t)$. The sampling interval $\Delta_t = \Delta_{\rm HF} = 0.005$ s, and the frequency resolution $\Delta_f = (M\Delta_t)^{-1}$. There have been many models proposed for $S_u(f)$ under the assumption of homogeneous, isotropic turbulence (Monin and Yaglom 1975; Azizyan et al. 1989) and Taylor's frozen hypothesis, which is well satisfied for short time intervals (Hill 1996). For stably stratified mixing layers, the assumption of isotropy is valid for estimates of energy dissipation rate when the buoyancy Reynolds number is larger than 100 (Smyth and Moum 2000). We assume the theoretical model from Azizyan et al. (1989), which was derived assuming a Gaussian cutoff function for the high-wavenumber region of the three-dimensional spectrum and can be written as

$$S_u(n\Delta_f) = 0.146\,169U^{2/3}\epsilon^{2/3}f^{-5/3}g[\beta(2\pi\eta f/U)^2], \qquad (23)$$

where $U$ is the mean velocity over the measurement time, $\epsilon$ is the energy dissipation rate, $\beta = 2.955\,18$,

$$\eta = \nu^{3/4}/\epsilon^{1/4} \qquad (24)$$

is the Kolmogorov microscale, $\nu$ is the kinematic viscosity, and

$$g(x) = (1 + x)\exp(-x) - \frac{11}{6}x^{5/6}\left(1 + \frac{6}{11}x\right)\Gamma\left(\frac{1}{6}, x\right), \qquad (25)$$

where

$$\Gamma(a, x) = \int_x^\infty t^{a-1}\exp(-t)\,dt \qquad (26)$$

is the incomplete Gamma function.

The kinematic viscosity is given by (NOAA 1976)

$$\nu = \frac{AT^{3/2}}{\rho(T + S)}, \qquad (27)$$

where $A = 1.458 \times 10^{-6}$ kg s$^{-1}$ m$^{-1}$ K$^{-1/2}$, $T$ is temperature in Kelvin, $\rho$ is the density of air, and $S = 110$ K is the Sutherland constant. To facilitate fitting to the data we write the spectral model as

$$S_u(n\Delta_f) = x_0 f^{-5/3} g\left\{\beta\left[\frac{2\pi\eta f(\nu/U)^{3/4}}{2.056\,74x_0^{3/8}}\right]^2\right\} + S_N, \qquad (28)$$

where $S_N$ is the spectral noise floor and

$$x_0 = 0.146169U^{2/3}\epsilon^{2/3}. \qquad (29)$$

The spectral model is a function of $x_0$, $\nu$, $S_N$, and $U$, or equivalently $\epsilon$, $\eta$, $S_N$, and $U$. The maximum likelihood estimate of $\epsilon$ is given by

$$\epsilon = (x_0/0.146169)^{3/2}/U, \qquad (30)$$

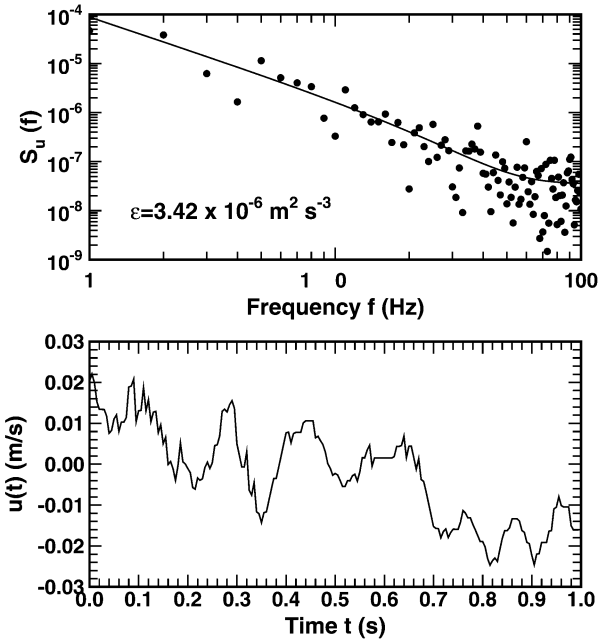


FIG. 8. Velocity fluctuations $u(t)$ and spectrum $S_u(f)$ with best-fit model (solid line) for low-turbulence regime.

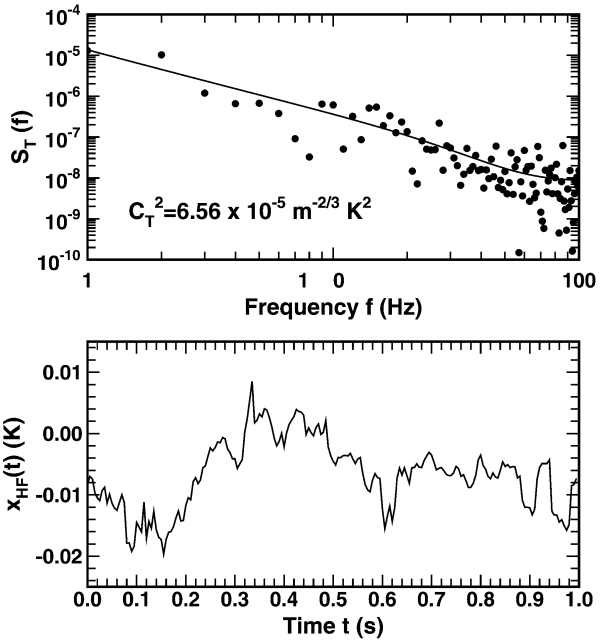


FIG. 9. Temperature fluctuations $x_{\mathrm{HF}}(t)$ and spectrum $S_T(f)$ with best-fit model (solid line) for the same low-turbulence regime of Fig. 8.

where $x_0$ is the maximum likelihood estimate of the spectral level (Smalikho 1997; Ruddick et al. 2000).

## 6. Temperature spectra

High-resolution measurements of the finescale temperature fluctuations were produced using the calibrated high-frequency signal $x_{\mathrm{HF}}(t)$ because the analog high-pass filter performs as an excellent detrending filter. The FFT estimate of the raw spectrum of the temperature fluctuations $x_{\mathrm{HF}}(t) = x_{\mathrm{HF}}(m\Delta_t)$ is

$$S_T(f) = S_T(n\Delta_f) = \frac{2\Delta_t}{M}\left|\sum_{m=0}^{M-1} x_{\mathrm{HF}}(m\Delta_t)e^{-2\pi inm/M}\right|^2, \quad (31)$$

which is normalized such that the integral of $S_T(f)$ over positive frequency is the variance of $x_{\mathrm{HF}}(t)$. The theoretical model for the one-dimensional temperature spectrum assuming locally homogeneous isotropic turbulence is produced from the three-dimensional model given by Eqs. (20), (23), and (49) of Frehlich (1992) following the analysis of Azizyan et al. (1989). The resulting spectrum can be written as

$$S_T(f) = 0.073\,084\,6U^{2/3}C_T^2 f^{-5/3}h(2\pi l_0 f/U), \quad (32)$$

where

$$l_0 = 5.79784\ \chi^{3/4}/\epsilon^{1/4} \quad (33)$$

is the temperature inner scale [defined as the intercept of the square-law dependence $r^2$ and inertial range dependence $r^{2/3}$; Tatarskii (1961)], $\chi$ is the thermal diffusivity of air, $U$ is the mean velocity over the measurement time, and

$$h(x) = (1 + 2.07x + 0.235\,667x^2)\exp(-x) + 0.006\,888\,89x^{5/3}\Gamma(1/3, x) \quad (34)$$

describes the Hill bump (Hill 1978). The thermal diffusivity of air is given by (NOAA 1976)

$$\chi = \frac{2.646\,38 \times 10^{-3}T^{3/2}}{\rho C_P(T + 245.4 \times 10^{-12/T})}, \quad (35)$$

where $T$ is average temperature in Kelvin, $\rho$ is the density of air, and $C_P = 1004$ J kg$^{-1}$ K$^{-1}$ is the specific heat of air at constant pressure. A useful approximation is

$$h(x) = (1 + 2.074\,72x + 0.235\,895x^2)\exp(-x). \quad (36)$$

The inner-scale $l_0$ is calculated from the best-fit $\epsilon$ and then $C_T^2$ is estimated from the best fit to the temperature spectrum. The spectral model is written as

$$S_T(f) = x_0 f^{-5/3}h(2\pi l_0 f/U) + S_N, \quad (37)$$

where

$$x_0 = 0.073\,084\,6\ U^{2/3}C_T^2, \quad (38)$$

and the maximum likelihood estimate of $C_T^2$ is

$$C_T^2 = \frac{x_0}{0.073\,084\,6U^{2/3}}, \quad (39)$$

where $x_0$ is the maximum likelihood estimate of the spectral level (Smalikho 1997; Ruddick et al. 2000). Examples of velocity and temperature spectra from 1 s of data for very weak turbulence are shown in Figs. 8 and 9, as well as the estimates for $\epsilon$ and $C_T^2$. The scatter reflects the statistical properties of the raw spectral estimates. Approximately $N = 50$ spectral points above

the noise floor are used for each estimate of $x_0$. Therefore, the estimation error for the estimates of $x_0$ ($C_T^2$ and $\epsilon^{2/3}$) is approximately $1/\sqrt{N}$ or 15% (Smalikho 1997). The spectral estimates at high frequency (50–100 Hz) are dominated by aliasing and the noise floor of the sensor. These 1-s estimates of $C_T^2$ and $\epsilon$ provide useful high-resolution measurements of the finescale turbulence structure in the atmospheric boundary layer and troposphere (Balsley et al. 2003). The fine-wire sensors are ideally suited for measurements in very low turbulence. During CASES-99, values of $\epsilon$ less than $10^{-7}$ $m^2\ s^{-3}$ and $C_T^2$ less than $10^{-6}$ $K^2\ m^{-2/3}$ were observed. The spectrum in Fig. 8 would have $\epsilon = 10^{-7}\ m^2\ s^{-3}$ if the spectral level was reduced by a factor of 10.536. Similarly, the spectrum in Fig. 9 would have $C_T^2 = 10^{-6}$ $K^2\ m^{-2/3}$ if the spectral level was reduced by a factor of 65.6. In both cases, there is sufficient spectral signal above the noise floor to produce an estimate. The accuracy of these estimates can be improved by computing spectra over longer time intervals (Muschinski et al. 2001).

## 7. Summary and discussion

Accurate finescale measurements of temperature and velocity are feasible for a tethered lifting system (TLS) using cold-wire and hot-wire sensors. The calibration of the cold-wire temperature sensor is produced using the fluctuations of a calibrated low-frequency solid-state temperature sensor. The absolute accuracy of the temperature measurements are typically better than 1 K. This limit was established by the drifting in the solid-state sensor with time. However, the accuracy of temperature fluctuations is typically much better because the gain of the solid-state sensor is very linear and stable with time. The accuracy of the slope of the temperature calibration is better than 2%. The hot-wire velocity sensor is calibrated by a modified King's law and a low-frequency measurement of the wind speed produced from a nearby Pitot tube vaned into the wind. The absolute accuracy is typically better than 1 $m\ s^{-1}$ and the accuracy of the slope of the calibration curve is better than 5%. Careful calibrations are required because the parameters of the modified King's law change with conditions.

The TLS is ideally suited for high-resolution measurements of finescale turbulence using multiple vertically spaced sensors. Accurate measurements of energy dissipation rate $\epsilon$ and temperature structure constant $C_T^2$ are possible with 1 s of data (see Figs. 8 and 9). The accuracy of Taylor's frozen hypothesis is very good over these short time intervals. The assumption that the hot-wire velocity is the longitudinal velocity $U(t)$ is valid when the local mean wind speed $U_0$ is large compared with the transverse velocity $v(t)$ [see Eq. (21)]. This is an excellent assumption for the low turbulence levels in the nocturnal jet and stable boundary layer. In addition, the errors from the transverse velocity are reduced for covariance and spectral estimates because they are second-order quantities. The random variations of $\epsilon$ and $C_T^2$ (global intermittency) are clearly observed (Balsley et al. 2003) since the accuracy of the estimates for the spectral level in the inertial range ($\epsilon^{2/3}$ and $C_T^2$) is typically 15% with 1 s of data. The assumption of local isotropy is required to estimate $\epsilon$ and $C_T^2$. This is a good assumption for high Reynold's number flows and a local description of turbulence described by Kolmogorov's refined similarity hypothesis (Kolmogorov 1962; Smyth and Moum 2000), that is, sufficiently small observation intervals (Sreenivasan and Stolovitzky 1996; Monin and Yaglom 1975).

Results from the TLS finescale turbulence measurements in the NBL are presented in Balsley et al. (2003). These include the observation of very large temperature gradients (28 $K\ m^{-1}$) over a few centimeters in altitude, large changes of turbulence intensity $C_T^2$ over a few meters in altitude, and very low levels of $C_T^2 \approx 10^{-5}$ $K^2\ m^{-2/3}$ extending over 60 m in altitude. The high-resolution TLS measurements are ideally suited for the statistical analysis of the variability of $\epsilon$ and $C_T^2$, as well as the spatial statistics of temperature and velocity in very low turbulence regions and regions of very high Reynolds number such as the middle of the convective mixed layer. Another important area of future work is the measurement of fluxes using improved platform angle and position sensors. New light-weight sensors of trace gases will permit accurate measurement of important fluxes for climate change and transport.

Recent advances in electronic circuits and flash memory will permit even higher data acquisition rates to fully resolve the dissipation range of turbulence. In addition, multiple hot-wire probes will produce measurements of all the components of the velocity vector. This will provide new information on the anisotropy of turbulence for many atmospheric phenomena at all altitudes from the surface to the free troposphere. The low effective mean velocity $U$ of the TLS (2–25 $m\ s^{-1}$) system compared with instrumented aircraft (100–200 $m\ s^{-1}$) permits more accurate measurements of the small-scale turbulence (Muschinski et al. 2001). Aircraft measurements are preferable when a large region of the atmosphere must be sampled for statistical accuracy, for example, with flux measurements. The TLS, on the other hand, has the advantage of multiple sensors, which provide instantaneous information in the vertical that is difficult to produce with aircraft measurements.

*Acknowledgments.* The authors acknowledge the suggestions of Andreas Muschinski and the excellent support from Steve Semmer, Cathy Jirak, Steve Oncley, and Tom Horst of the NCAR calibration facility. This work was supported by NSF and ARO.

REFERENCES

Alisse, J., and C. Sidi, 2000: Experimental probability density functions of small-scale fluctuations in the stably stratified atmosphere. *J. Fluid Mech.*, **402,** 137–162.

Azizyan, G. V., B. M. Koprov, and V. V. Kalugin, 1989: Spectra of turbulent velocity fluctuations in the viscous range. *Izv. Atmos. Oceanic Phys.,* **25,** 935–938.

Balsley, B. B., M. L. Jensen, and R. G. Frehlich, 1998: The use of state-of-the-art kites for profiling the lower atmosphere. *Bound.-Layer Meteor.,* **87,** 1–25.

——, R. G. Frehlich, M. L. Jensen, Y. Meillier, and A. Muschinski, 2003: Extreme gradients in the nocturnal boundary layer: Structure, evolution, and potential causes. *J. Atmos. Sci.,* **60,** 2496–2508.

Bruun, H. H., 1995: *Hot-Wire Anemometry.* Oxford University Press, 532 pp.

Cohn, S. A., 1995: Radar measurements of turbulent eddy dissipation rate in the troposphere: A comparison of techniques. *J. Atmos. Oceanic Technol.,* **12,** 85–95.

Cuijpers, J. W. M., and W. Kohsiek, 1989: Vertical profiles of the structure parameter of temperature in the stable, nocturnal boundary layer. *Bound.-Layer Meteor.,* **47,** 111–129.

Danaila, L., F. Anselmet, and R. A. Antonia, 2002: An overview of the effect of large-scale inhomogeneities on small-scale turbulence. *Phys. Fluids,* **14,** 2475–2484.

Eaton, F. D., S. A. McLaughlin, and J. R. Hines, 1995: A new frequency-modulated continuous wave radar for studying planetary boundary layer morphology. *Radio Sci.,* **30,** 75–88.

Frehlich, R., 1992: Laser scintillation measurements of the temperature spectrum in the atmospheric surface layer. *J. Atmos. Sci.,* **49,** 1494–1509.

——, S. M. Hannon, and S. W. Henderson, 1998: Coherent Doppler lidar measurements of wind field statistics. *Bound.-Layer Meteor.,* **86,** 233–256.

Garratt, J. R., 1981: Observations in the nocturnal boundary layer. *Bound.-Layer Meteor.,* **22,** 21–48.

Gossard, E. E., W. D. Neff, R. J. Zamora, and J. E. Gaynor, 1984: The fine structure of elevated refractive layers: Implications for over-the-horizon propagation and radar sounding systems. *Radio Sci.,* **19,** 1523–1533.

Hill, R. J., 1978: Models of the scalar spectrum for turbulent advection. *J. Fluid Mech.,* **88,** 541–562.

——, 1996: Corrections to Taylor's frozen turbulence approximation. *Atmos. Res.,* **40,** 153–175.

Hugo, R. J., S. R. Nowlin, F. D. Eaton, K. P. Bishop, and K. A. McCrae, 1999: Hot-wire calibration in a non-isothermal incompressible pressure variant flow. *Proc. SPIE,* **3706,** 11–22.

Jacoby-Koaly, S., B. Campistron, S. Bernard, B. Bénech, F. Ardhuin-Girard, J. Dessens, E. Dupont, and B. Carissimo, 2002: Turbulent dissipation rate in the boundary layer via UHF wind profiler Doppler spectral width measurements. *Bound.-Layer Meteor.,* **103,** 361–389.

Kolmogorov, A. N., 1962: A refinement of previous hypotheses concerning the local structure turbulence in a viscous incompressible fluid at high Reynolds number. *J. Fluid. Mech.,* **13,** 82–85.

Mahrt, L., 1985: Vertical structure and turbulence in the very stable boundary layer. *J. Atmos. Sci.,* **42,** 2333–2349.

——, 1989: Intermittency of atmospheric turbulence. *J. Atmos. Sci.,* **46,** 79–95.

——, and N. Gamage, 1987: Observations of turbulence in stratified flow. *J. Atmos. Sci.,* **44,** 1106–1121.

Miller, D. O., C. Tong, and J. C. Wyngaard, 1999: The effects of probe-induced flow distortions on velocity covariances: Field observations. *Bound.-Layer Meteor.,* **91,** 483–493.

Monin, A. S., and A. M. Yaglom, 1975: *Statistical Fluid Mechanics: Mechanics of Turbulence.* Vol. 2. MIT Press, 874 pp.

Muschinski, A., and C. Wode, 1998: First in situ evidence for coexisting submeter temperature and humidity sheets in the lower free troposphere. *J. Atmos. Sci.,* **55,** 2893–2906.

——, and D. H. Lenschow, 2001: Future directions for research on meter- and submeter-scale atmospheric turbulence. *Bull. Amer. Meteor. Soc.,* **82,** 2831–2843.

——, R. Frehlich, M. L. Jensen, R. Hugo, A. Hoff, F. Eaton, and B. Balsley, 2001: Fine-scale measurements of turbulence in the lower troposphere: An intercomparison between a kite- and balloon-borne, and a helicopter-borne measurement system. *Bound.-Layer Meteor.,* **98,** 219–250.

Nieuwstadt, F. T. M., 1984a: The turbulent structure of the stable, nocturnal boundary layer. *J. Atmos. Sci.,* **41,** 2202–2216.

——, 1984b: Some aspects of the turbulent stable boundary layer. *Bound.-Layer Meteor.,* **30,** 31–55.

NOAA, 1976: U.S. Standard Atmosphere 1976. National Oceanic and Atmospheric Administration, NOAA-S/T 76-1562, 227 pp. [Available from the National Technical Information Office, Springfield, VA 22161 (Product number: ADA-035-6000).]

Poulos, G. S., and Coauthors, 2002: CASES-99: A comprehensive investigation of the stable nocturnal boundary layer. *Bull. Amer. Meteor. Soc.,* **83,** 555–581.

Richter, J. H., 1969: High resolution tropospheric radar sounding. *Radio Sci.,* **4,** 1261–1268.

Ruddick, B., A. Anis, and K. Thompson, 2000: Maximum likelihood spectral fitting: The Batchelor spectrum. *J. Atmos. Oceanic Technol.,* **17,** 1541–1555.

Skelly, B. T., D. R. Miller, and T. H. Meyer, 2002: Triple-hot-film anemometer performance in CASES-99 and a comparison with sonic anemometer measurements. *Bound.-Layer Meteor.,* **105,** 275–304.

Smalikho, I. N., 1997: Accuracy of the turbulent energy dissipation rate estimation from the temporal spectrum of wind fluctuations. *Atmos. Oceanic Opt.,* **10,** 559–563.

Smedman, A.-S., 1988: Observation of a multi-level turbulence structure in a very stable atmospheric boundary layer. *Bound.-Layer Meteor.,* **44,** 231–253.

——, H. Bergstrom, and U. Hogstrom, 1995: Spectral variances and length scales in a marine stable boundary layer dominated by a low level jet. *Bound.-Layer Meteor.,* **76,** 211–232.

Smyth, W. D., and J. N. Moum, 2000: Anisotropy of turbulence in stably stratified mixing layers. *Phys. Fluids,* **12,** 1343–1362.

Sreenivasan, K. R., and G. Stolovitzky, 1996: Statistical dependence of inertial range properties on large scales in a high-Reynolds-number shear flow. *Phys. Rev. Lett.,* **77,** 2218–2221.

Tatarskii, V. I., 1961: *Wave Propagation in a Turbulent Medium.* McGraw-Hill, 285 pp.

Wyngaard, J. C., and B. Kosovic, 1994: Similarity of structure-function parameters in the stably stratified boundary layer. *Bound.-Layer Meteor.,* **71,** 277–287.